Article

Effect of Molybdenum Additives on Corrosion Behavior of (CoCrFeNi)$_{100-x}$Mo$_x$ High-Entropy Alloys

Wenrui Wang [1,*], Jieqian Wang [1], Honggang Yi [1], Wu Qi [1] and Qing Peng [2]

[1] School of Mechanical Engineering, University of Science and Technology Beijing, Beijing 100083, China; jieqian.wang@xs.ustb.edu.cn (J.W.); hg.yi@ustb.edu.cn (H.Y.); wu.qi@xs.ustb.edu.cn (W.Q.)

[2] Nuclear Engineering and Radiological Sciences, University of Michigan, Ann Arbor, MI 48109, USA; qpeng@umich.edu

* Correspondence: gmbitwrw@ustb.edu.cn; Tel.: +86 010-6233-4845

Abstract: The present work investigates the influence of micro-alloyed Mo on the corrosion behavior of (CoCrFeNi)$_{100-x}$Mo$_x$ high-entropy alloys. All of the (CoCrFeNi)$_{100-x}$Mo$_x$ alloys exhibit a single face-centered cubic (FCC) solid solution. However, the (CoCrFeNi)$_{97}$Mo$_3$ alloy exhibits an ordered sigma (σ) phase enriched in Cr and Mo. With the increase of x (the Mo content) from 1 to 3, the hardness of the (CoCrFeNi)$_{100-x}$Mo$_x$ alloys increases from 124.8 to 133.6 Vickers hardness (HV), and the compressive yield strength increases from 113.6 MPa to 141.1 MPa, without fracture under about a 60% compressive strain. The potentiodynamic polarization curve in a 3.5% NaCl solution indicates that the addition of Mo has a beneficial effect on the corrosion resistance to some certain extent, opposed to the σ phase. Furthermore, the alloys tend to form a passivation film in the 0.5 M H$_2$SO$_4$ solution in order to inhibit the progress of the corrosion reaction as the Mo content increases.

Keywords: (CoCrFeNi)$_{100-x}$Mo$_x$ alloys; high entropy alloy; microstructure; mechanical properties; corrosion behavior

1. Introduction

Traditional alloys only have one major element as a matrix [1]. With the increase of the amount of alloying elements and the concentration of minor elements, the alloy forms a fragile intermetallic phase, which not only increases the difficulty of the microstructure, but also may result in a reduction in the mechanical performance [2–4]. To overcome these difficulties, high entropy alloys (HEAs) are invented with extensive research interests; HEAs usually compose of five or more kinds of major elements, with the concentration of each principal element being between 5 and 35 at % [5–7]. HEAs tend to generate a face-centered cubic (FCC), body-centered cubic (BCC), or hexagonal closed-packed (HCP) multicomponent solid solution phase [8,9]. Some HEAs have been confirmed to achieve a series of excellent properties, such as high strength, high hardness, and glorious corrosion resistance [10–12].

The CoCrFeNi alloy has received extensive attention for its outstanding corrosion resistance, ductility, and structure stability [13,14]. However, because of the poor mechanical strength, the application of the CoCrFeNi alloy in engineering has been limited. It has been shown that an ordered σ strengthening phase can be formed by a certain amount of Mo additives, resulting in precipitation strengthening [15–17]. However, the excessive addition of Mo causes a large amount of the coarse σ strengthening phase, which may lead to a rapid increase of the alloy brittleness. Furthermore, because of the low electronic potential of Mo, the excessive content of Mo may reduce the corrosion resistance [18–20]. Referring to the chemical composition of austenitic stainless steel, the content of Mo in stainless steel is generally less than 3 wt %. Therefore, we also supply a small

amount of Mo in addition to the CoCrFeNi alloy, in order to study the corrosion resistance of the $(CoCrFeNi)_{100-x}Mo_x$ alloy for the development of an HEA system, with a good performance of both strength and corrosion resistance.

In this paper, the as-cast $(CoCrFeNi)_{100-x}Mo_x$ (x =1, 2, and 3 wt %) HEAs have been prepared mainly by vacuum arc melting. The excellent corrosion behavior was investigated by the electrochemical experiments.

2. Materials and Methods

2.1. Samples Fabrication

Elements Co, Cr, Fe, Ni, and Mo with purities of over 99.9 wt % were prepared as raw materials previously. The as-cast $(CoCrFeNi)_{100-x}Mo_x$ (x = 1, 2, and 3, represented by Mo_1, Mo_2, and Mo_3, respectively) were prepared by vacuum arc melting and were fabricated under the WK-∏ vacuum arc melting furnace at least five times in the crucible, so as to ensure the chemical homogeneity. The size of the ingot was approximately Φ 35 × 10 mm, and the ingot was annealed for 3 h under 500 °C and was cooled in the air so as to release the residual stress caused by rapid cooling during casting.

2.2. Microstructure of the $(CoCrFeNi)_{100-x}Mo_x$ Alloys

The crystalline phases of the $(CoCrFeNi)_{100-x}Mo_x$ alloys were identified by X-ray diffraction (XRD), using an Ultima IV X-ray diffractometer with Cu K_α radiation. The X-ray diffractometer has an operating voltage of 30 kV and an operating current of 20 mA with the diffraction angle (2θ) from 20 to 90°, at a scanning rate of 4°/min.

Etching the $(CoCrFeNi)_{100-x}Mo_x$ alloys with aqua regia (HNO_3: HCl = 1:3, volume fraction) and using FE-SEM JEOL JEM-7600F scanning-electron microscopy (SEM) (JEOL Ltd., Tokyo, Japan) equipped with an energy dispersive spectrometer (EDS) allowed for an analysis of the microstructure and composition.

2.3. Mechanical Properties

The microhardness was measured using a Wolpert-401MVD Vickers hardness tester (WOLPERT Co., Norwood, MA, USA) with loads of 500 g and a duration of 10 s. The measurements were performed at 10 different locations on each sample, and the average value of the 10 measurements was calculated. Compressive tests were carried out on the Φ 3 × 6 mm samples, using the universal testing machine (CMT 4305) (MTS Co., Eden Prairie, MN, USA) with a strain rate of 10^{-3} s^{-1}.

2.4. Electrochemical Corrosion Test

The electrochemical experiments were performed on $(CoCrFeNi)_{100-x}Mo_x$ alloys, using the Potentiostat Workstation Versa STAT MC (PARSTAT 4000, AMETEK Co., Princeton, NJ, USA). A three-electrode electrochemical cell using a saturated calomel electrode (SCE) as a reference electrode, a platinum plate as an auxiliary electrode, and a sample as a working electrode were tested. The electrochemical experiments of the $(CoCrFeNi)_{100-x}Mo_x$ alloys were conducted in a 3.5% NaCl and 0.5 M H_2SO_4 solution at room temperature, respectively. The potentiodynamic polarization measurements were taken at a scan rate of 1 mV/s from a potential scanning range of −0.5 V to 1.1 V.

2.5. Corroded Microstructure

The electrochemically tested alloys were cleaned using an ultrasonic cleaner, and then dried in nitrogen. SEM and EDS were used to study the morphology of the corrosion surface of the high-entropy alloys.

3. Results and Discussion

3.1. Microstructure of the (CoCrFeNi)$_{100-x}$Mo$_x$ Alloys

Figure 1 represents the XRD pattern of the (CoCrFeNi)$_{100-x}$Mo$_x$ (x = 1, 2, 3) alloys. All of the samples of alloys have a single FCC solid solution structure, which was confirmed by the predecessors [21]. As the Mo content increases, the peak intensity changes, but the FCC phase is kept. As the Mo content becomes 3 wt % (Mo$_3$ structure), the small peak on the left of the matrix FCC phase in the XRD patterns is identified as Cr and Mo rich σ phase, which agrees with the previous remarks [22].
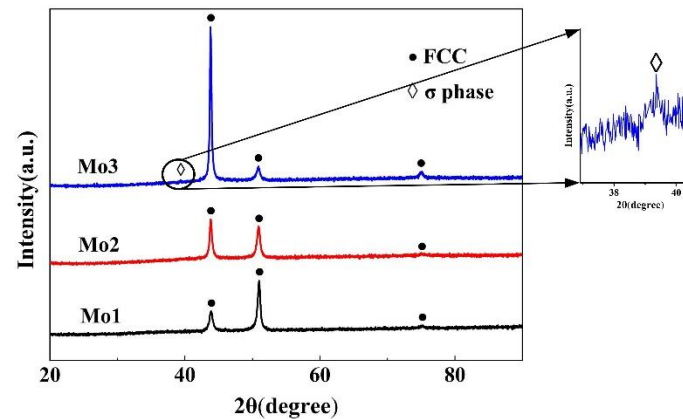

Figure 1. XRD (X-ray diffraction) patterns of the (CoCrFeNi)$_{100-x}$Mo$_x$ (x = 1, 2, 3) high entropy alloys.

The SEM images of the (CoCrFeNi)$_{100-x}$Mo$_x$ (x = 1, 2, and 3) alloys presented in Figure 2 shows that the alloys are composed of typical dendritic structures. Region A is interdendrites and region B is dendrites. Figure 2c presents the SEM image of the Mo$_3$ alloy, and region D is the grain boundary. Figure 2d is a part of the SEM of the Mo$_3$ alloy. The EDS results of the (CoCrFeNi)$_{100-x}$Mo$_x$ alloys are shown in Table 1. According to the EDS, the dendrite is the Co and Fe rich phase, and the interdendrite is the Cr and Mo rich phase. Combined with the XRD and EDS results, the Mo$_3$ alloy exhibits Cr and Mo rich σ phase in the interdendrite. When the content of Mo is 1 and 2 wt %, there is no formation of a precipitate phase in the alloy because of the high entropy effect. However, HEAs undergo spinodal decomposition inside the crystal grains during cooling, leading to the formation of microstructures with the same structure but different compositions.
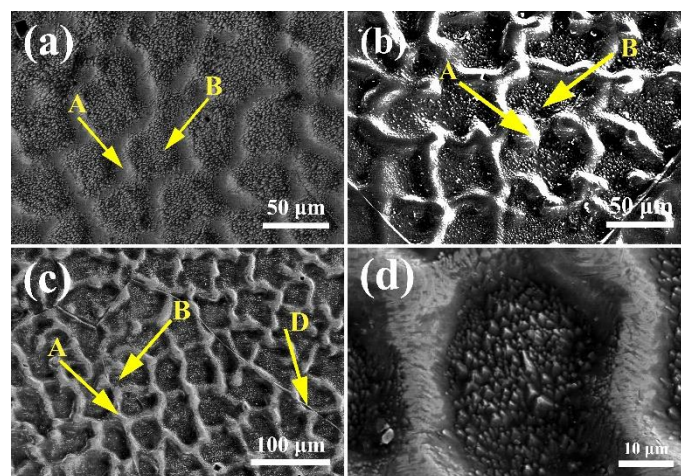

Figure 2. SEM (scanning-electron microscopy) images of the (CoCrFeNi)$_{100-x}$Mo$_x$ high-entropy alloys:
(**a**) x = 1; (**b**) x = 2; (**c**) x = 3; (**d**) 10 × magnification.

Table 1. Element concentration determined using the energy dispersive spectrometer (EDS) of the three samples of the $(CoCrFeNi)_{100-x}Mo_x$ alloys (at %).

Element		Cr	Fe	Co	Ni	Mo
Mo_1	Dendrite	25.25	23.54	26.07	24.53	0.61
	interdendrite	27.69	22.31	24.03	24.94	1.04
Mo_2	Dendrite	26.02	25.17	24.55	23.56	0.69
	interdendrite	27.20	23.20	23.33	23.87	2.40
Mo_3	Dendrite	24.99	23.47	25.28	24.96	1.31
	interdendrite	26.82	22.54	24.81	24.35	1.50

3.2. Mechanical Properties

Figure 3 shows the Vickers hardness (HV) of the $(CoCrFeNi)_{100-x}Mo_x$ alloys as a function of the Mo content. The alloy hardness increases from 124.83 to 133.60 HV, with the Mo content increasing from 1 to 3 wt %. When the content of the Mo element is 3 wt %, the presence of the σ phase results in a remarkable increase in the hardness.
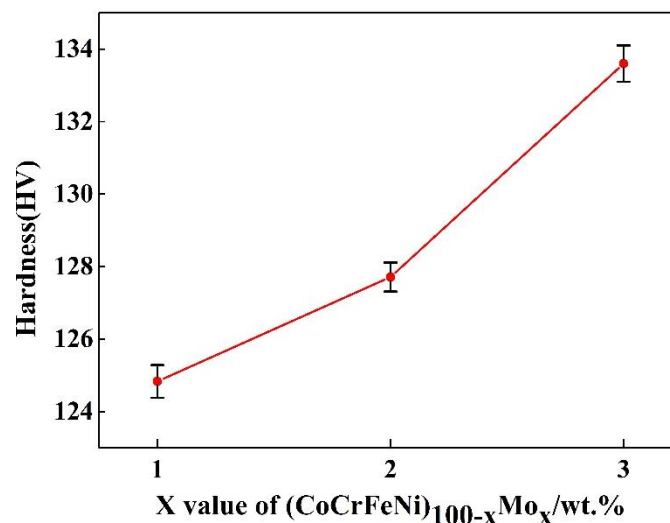
Figure 3. Vickers hardness of the $(CoCrFeNi)_{100-x}Mo_x$ high-entropy alloys as a function of the Mo content.

Besides the hardness, we have examined the stress–strain relationships. The compressive stress–strain curves and the inner longitudinal-section SEM images of the $(CoCrFeNi)_{100-x}Mo_x$ (x = 1, 2, and 3) alloys are shown in Figure 4. After yielding, the strength of the alloys increases continuously. All of the three samples do not break under about a 60% compressive strain, indicating that the alloys possess a good ductility, flexibility, and fracture strain. As shown in Figure 4b–d, the deformation of the Mo_3 subgrain boundaries is more prominent in the angle of 45°, probably due to the resolved shear stress.

Table 2 lists the mechanical properties of the $(CoCrFeNi)_{100-x}Mo_x$ alloys. The Mo_1 and Mo_2 alloys exhibit a similar behavior. The yield stress of the Mo_3 alloy increases significantly because of the second-phase hardening by the σ phase, as reported in the literature [23,24].
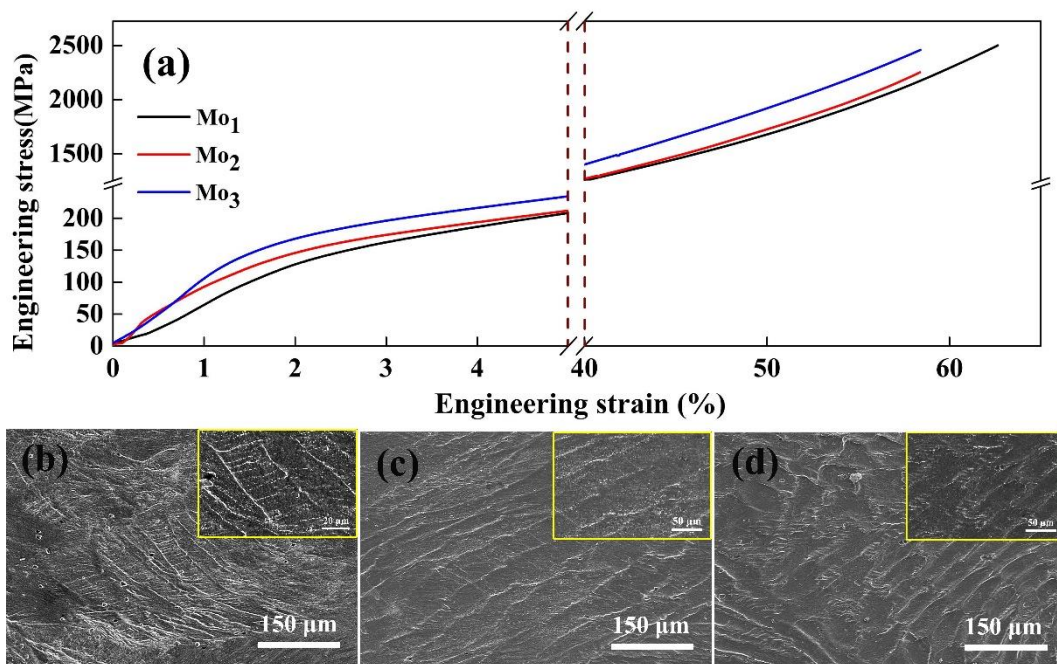
Figure 4. (**a**) Compressive stress–strain curves and the inner longitudinal-section SEM images of the $(CoCrFeNi)_{100-x}Mo_x$ alloys after compression deformation: (**b**) $x = 1$; (**c**) $x = 2$; (**d**) $x = 3$.

Table 2. Mechanical properties (yield stress, compressive strength, and fracture strain) of the $(CoCrFeNi)_{100-x}Mo_x$ alloys for $x = 1, 2,$ and 3 as Mo_1, Mo_2, and Mo_3, respectively.

Alloy	Yield Stress σ_y (MPa)	Compressive Strength σ_{max} (MPa)	Fracture Strain ε_p (%)
Mo_1	113.6	Not fractured	>60
Mo_2	119.7	Not fractured	>60
Mo_3	141.1	Not fractured	>60

3.3. Environmental Effect on Corrosion Behavior

3.3.1. Corrosion Behavior in Chloride-Containing Solutions

Figure 5 lists the polarization curve of the $(CoCrFeNi)_{100-x}Mo_x$ ($x = 1, 2,$ and 3) alloys in a 3.5% NaCl solution. The corrosion potential of the alloys gradually shifts to more positive potentials with a decreasing Mo content.

Table 3 presents the electrochemical parameters of the $(CoCrFeNi)_{100-x}Mo_x$ ($x = 1, 2,$ and 3) alloys in a 3.5% NaCl solution. The corrosion current densities (i_{corr}) of the Mo_1, Mo_2, and Mo_3 alloys were 0.4, 0.24, and 6.6 $\mu A/cm^2$, and the corrosion potentials (E_{corr}) were -199, -277, and -493 mV, respectively. The breakdown potential (E_b) gradually shifts to more positive potentials. E_{pit} is a primary passivation potential. ΔE is the passive region width, defined as the difference between the E_b and E_{pit}. The i_{corr} value of the Mo_3 alloy is an order of magnitude higher than the other two. The corrosion resistance of Mo_3 was dropped. Therefore, the presence of the Cr and Mo rich σ phase in the Mo_3 alloy leads to the diminution of the corrosion resistance.
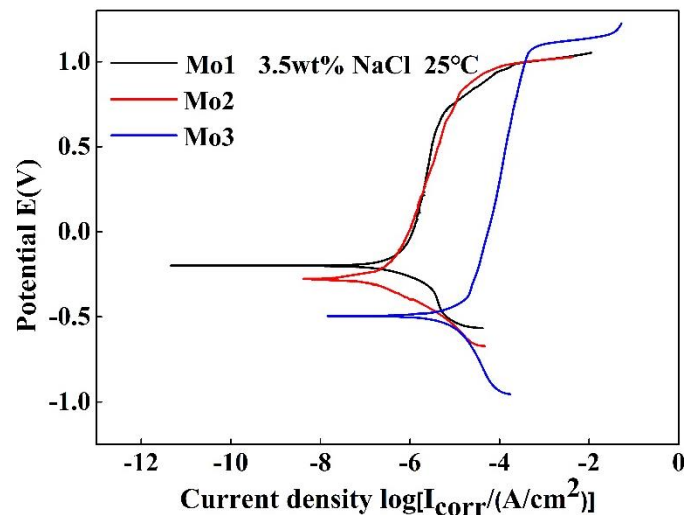
Figure 5. Polarization curves of the $(CoCrFeNi)_{100-x}Mo_x$ (x = 1, 2, and 3) alloys in a 3.5% NaCl solution.

Table 3. Electrochemical parameters of the $(CoCrFeNi)_{100-x}Mo_x$ alloys in a 3.5% NaCl solution.

Alloy	E_{corr} (mV)	I_{corr} (μA/cm^2)	E_b (mV)	E_{pit} (mV)	ΔE (mV)
Mo$_1$	−199	0.402	992	−5	997
Mo$_2$	−277	0.235	968	−108	1076
Mo$_3$	−493	6.610	1053	−358	1411

Figure 6 presents the microstructure of the $(CoCrFeNi)_{100-x}Mo_x$ alloys after potentiodynamic polarization in a 3.5% NaCl solution. DR is dendrite and IR is interdendrite. According to the SEM images, the majority of types of corrosion were mainly the pitting corrosion. The Mo$_3$ alloy is more susceptible to pitting corrosion, which is consistent with the polarization curve results. Region A is a Cr-rich phase and region B is a Mo-rich phase. There is an element of segregation that causes the corrosion to occur. The interdendritic phase of Mo$_3$ is the Cr- and Mo-rich phase, and the dendrite is a Cr- and Mo-depleted phase. Therefore, galvanic corrosion occurred at the junctions of dendrites. The XRD and SEM result show that the Mo and Cr rich σ phase appeared inside the interdendrite, the corrosion occurred at the interfaces around σ phase, as shown in Figure 6c,d. The results of the EDS of the alloy after corrosion are summarized in Table 4.
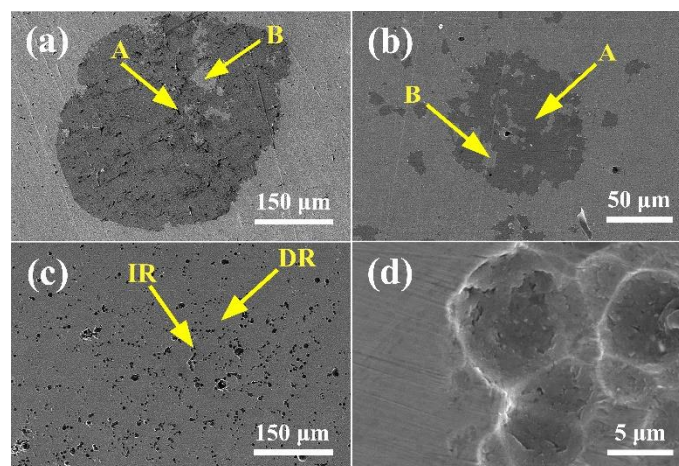

Figure 6. SEM images of $(CoCrFeNi)_{100-x}Mo_x$ after potentiodynamic polarization in a 3.5% NaCl solution: (**a**) x = 1; (**b**) x = 2; (**c**) x = 3; (**d**) the interdendrite morphology of the Mo$_3$ alloy.

Table 4. EDS results for the Mo_3 alloy after the potentiodynamic polarization in a 3.5% NaCl solution.

Element	Region	Cr (%)	Fe (%)	Co (%)	Ni (%)	Mo (%)
Mo_1	A	26.17	24.56	23.32	25.01	0.93
	B	30.79	23.79	22.87	22.51	0.04
Mo_2	A	26.44	23.72	24.32	23.83	1.70
	B	35.81	23.79	19.78	20.11	0.52
Mo_3	DR	24.96	25.21	24.72	24.88	0.23
	IR	29.06	23.21	22.43	22.76	2.54

3.3.2. Corrosion Behavior in Acid Solutions

Figure 7 shows the polarization curve of the $(CoCrFeNi)_{100-x}Mo_x$ (x = 1, 2, and 3) alloys in 0.5 M H_2SO_4. Table 5 presents the electrochemical parameters of the $(CoCrFeNi)_{100-x}Mo_x$ (x = 1, 2, and 3) alloys in 0.5 M H_2SO_4. The i_{pp} is the lunt current density. It can be seen from the electrochemical parameters that the i_{corr} was 34.1, 28.0, and 15.4 µA/cm^2, respectively. The E_{corr} shifted to more positive potentials, and the i_{corr} value dropped as the Mo content increased. This suggests that the alloys tend to form a passivation film to inhibit the progress of the corrosion reaction.
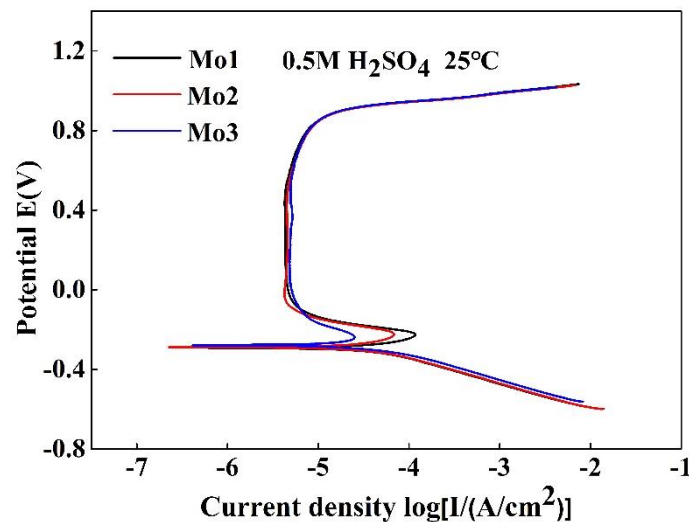
Figure 7. Polarization curves of the $(CoCrFeNi)_{100-x}Mo_x$ (x = 1, 2, and 3) alloys in a 0.5 M H_2SO_4 solution

Table 5. Electrochemical parameters of the $(CoCrFeNi)_{100-x}Mo_x$ alloys in a 0.5 M H_2SO_4 solution.

Alloy	E_{corr} (mV)	I_{corr} (µA/cm^2)	E_{pp} (mV)	i_{pp} (µA/cm^2)	ΔE (mV)
Mo_1	−294	34.1	−225	117	655
Mo_1	−290	28.0	−225	68	681
Mo_1	−279	15.4	−239	25	751

Figure 8 shows the SEM microstructure of the $(CoCrFeNi)_{100-x}Mo_x$ alloys after potentiodynamic polarization in a 0.5 M H_2SO_4 solution, combined with EDS, because the low potential of Mo is enriched and the Cr_2O_3 is insufficient in region A. Consequently, region A is more susceptible to corrosion in the H_2SO_4 solution. When the content of Mo is 3 wt %, as Figure 8c indicates, the results of the EDS analysis show that the concentration of element Cr in region A is reduced, and the content of Mo in region B is significantly higher than that in region A, the effect of Mo was to form Mo (VI) oxyhydroxide or molybdate (MoO_4^{2-}), decreasing the rate of dissolution in active zones. Hence, the corrosion of the Mo_3 alloy is concentrated in region A.
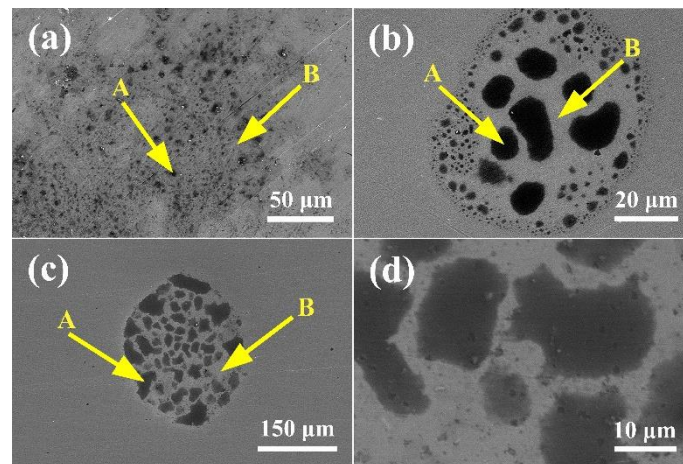
Figure 8. SEM images of $(CoCrFeNi)_{100-x}Mo_x$ after potentiodynamic polarization in a 0.5 M H_2SO_4 solution: (**a**) $x = 1$; (**b**) $x = 2$; (**c**) $x = 3$; (**d**) partial view of the Mo_3 alloy.

Figure 9a shows the comparison of the corrosion behavior between the HEAs and the conventional corrosion resistant alloys in a 3.5% NaCl solution, compared with those of the conventional corrosion resistant alloys [25,26]. The HEAs are located in the upper part of Figure 9a, the E_{corr} of the HEAs are more positive than those of the Mn alloys, Ni alloys, and some of the Ti alloys. On the other hand, the i_{corr} of the HEAs are much lower than some of Mn alloys and are comparable with the Ti alloys, which indicates that the corrosion resistance of the HEAs is comparable or even better than those of the conventional alloys. However, the partial i_{corr} of the HEAs is higher than that of the total, because the presence of the σ phase is catastrophic for HEAs. Figure 9b presents the comparison of the corrosion behavior between the HEAs and the conventional corrosion resistant alloys in the 0.5 M H_2SO_4 solution. Compared with the conventional alloys [27,28], the E_{corr} of the HEAs are much more positive than those of the Ti alloys and Ni alloys. The i_{corr} of the HEAs are much lower than the Ti alloys, Ni alloys, and some of the Cu alloys. As a general trend, the corrosion resistance of the HEAs in the 0.5 M H_2SO_4 solution is better than those of the conventional alloys.
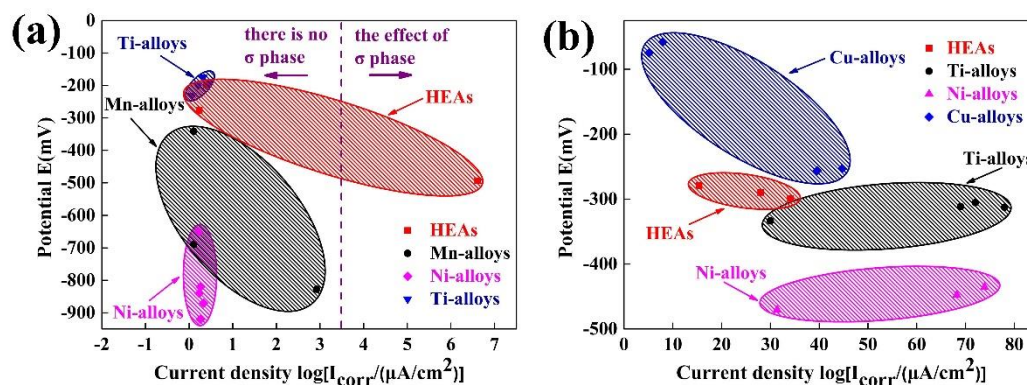

Figure 9. Comparison of the i_{corr} and E_{corr} between high entropy alloys (HEAs) and conventional alloys: (**a**) in a 0.5 M NaCl solution; (**b**) in a 0.5 M H_2SO_4 solution.

4. Conclusions

The $(CoCrFeNi)_{100-x}Mo_x$ ($x = 1$, 2, and 3) alloys have been synthesized. Their microstructures, mechanical properties, and corrosion behaviors have been experimentally investigated. The microstructures of the $(CoCrFeNi)_{100-x}Mo_x$ ($x = 1$, 2, and 3) alloys belong to a single FCC structure. The increase in Mo promotes the formation of the Cr- and Mo-rich σ phase. The hardness and compressive yield strength increase obviously with an increase of the Mo content from 1 to 3 wt %. Regarding the potentiodynamic polarization curves of the $(CoCrFeNi)_{100-x}Mo_x$ alloys in a 3.5% NaCl solution, the

curves of the Mo_1 and Mo_2 alloys indicated that the increase of the Mo content increases the corrosion resistance of the chloride environment to some extent. However, the Cr and Mo rich σ phase is present at the grain boundary of the Mo_3 alloy, resulting in a decreasing in corrosion resistance in the 3.5% NaCl solution. Furthermore, the potentiodynamic polarization curves of the $(CoCrFeNi)_{100-x}Mo_x$ alloys in the 0.5 M H_2SO_4 solution yielded an extensive passive region, and as the content of the Mo increased, the corrosion current density gradually decreased. Therefore, in an acidic solution, the addition of Mo has a positive effect on the corrosion resistance of the $(CoCrFeNi)_{100-x}Mo_x$ alloys.

Author Contributions: Conceptualization, W.W.; formal analysis, J.W.; methodology, J.W. and W.Q.; resources, W.W.; writing (original draft), J.W.; writing (review and editing), J.W., H.Y. and Q.P.

Conflicts of Interest: The authors declare no conflict of interest.

References

1.　Peng, Q.; Meng, F.; Yang, Y.; Lu, C.; Deng, H.; Wang, L.; De, S.; Gao, F. Shockwave generates <100> dislocation loops in bcc iron. *Nat. Commun.* **2018**, *9*, 4880. [CrossRef] [PubMed]

2.　Ye, Q.; Feng, K.; Li, Z.; Lu, F.; Li, R.; Huang, J.; Wu, Y. Microstructure and corrosion properties of CrMnFeCoNi high entropy alloy coating. *Appl. Surface Sci.* **2017**, *396*, 1420–1426. [CrossRef]

3.　Shun, T.T.; Chang, L.Y.; Shiu, M.H. Age-hardening of the $CoCrFeNiMo_{0.85}$ high-entropy alloy. *Mater. Charact.* **2013**, *81*, 92–96. [CrossRef]

4.　Senkov, O.N.; Zhang, F.; Miller, J.D. Phase composition of a $CrMo_{0.5}NbTa_{0.5}TiZr$ high entropy alloy: Comparison of experimental and simulated data. *Entropy* **2013**, *15*, 3796–3809. [CrossRef]

5.　Qiu, X.W.; Zhang, Y.P.; He, L.; Liu, C.-G. Microstructure and corrosion resistance of AlCrFeCuCo high entropy alloy. *J. Alloys Compd.* **2013**, *549*, 195–199. [CrossRef]

6.　Zhang, Y.; Tang, T.T.Z.Z.; Gao, M.C.; Dahmen, K.A.; Liaw, P.K.; Lu, Z.P. Microstructures and properties of high-entropy alloys. *Prog. Mater. Sci.* **2014**, *61*, 1–93. [CrossRef]

7.　Tung, C.C.; Yeh, J.W.; Shun, T.-T.; Chen, S.K.; Huang, Y.S.; Chen, H.C. On the elemental effect of AlCoCrCuFeNi high-entropy alloy system. *Mater. Lett.* **2007**, *61*, 1–5. [CrossRef]

8.　Yeh, J.W. Recent progress in high entropy alloys. *Ann. Chim. Sci. Mat.* **2006**, *31*, 633–648. [CrossRef]

9.　Zhang, H.; Pan, Y.; He, Y.Z. Synthesis and characterization of FeCoNiCrCu high-entropy alloy coating by laser cladding. *Mater. Des.* **2011**, *32*, 1910–1915. [CrossRef]

10.　Chen, Y.; Duval, T.; Hung, U.; Yeh, J.; Shih, H. Microstructure and electrochemical properties of high entropy alloys—A comparison with type-304 stainless steel. *Corros. Sci.* **2005**, *47*, 2257–2279. [CrossRef]

11.　Qiu, X.-W.; Wu, M.J.; Liu, C.G.; Zhang, Y.P.; Huang, C.-X. Corrosion performance of $Al_2CrFeCoxCuNiTi$ high-entropy alloy coatings in acid liquids. *J. Alloys Compd.* **2017**, *708*, 353–357. [CrossRef]

12.　Zhang, Y.; Yan, X.H.; Liao, W.B.; Zhao, K. Effects of nitrogen content on the structure and mechanical properties of $(Al_{0.5}CrFeNiTi_{0.25})$ N_x high-entropy films by reactive sputtering. *Entropy* **2018**, *20*, 624. [CrossRef]

13.　Hsu, Y.J.; Chiang, W.C.; Wu, J.K. Corrosion behavior of $FeCoNiCrCu_x$ high-entropy alloys in 3.5% sodium chloride solution. *Mater. Chem. Phys.* **2005**, *92*, 112–117. [CrossRef]

14.　Shi, Y.; Yang, B.; Liaw, P.K. Corrosion-resistant high-entropy alloys: A review. *Metals* **2017**, *7*, 43. [CrossRef]

15.　Zhu, J.; Zhang, H.; Fu, H.; Wang, A.; Li, H.; Hu, Z. Microstructures and compressive properties of multicomponent $AlCoCrCuFeNiMo_x$ alloys. *J. Alloys Compd.* **2010**, *497*, 52–56. [CrossRef]

16.　Zhu, J.; Fu, H.; Zhang, H.; Wang, A.; Li, H.; Hu, Z. Microstructures and compressive properties of multicomponent $AlCoCrFeNiMo_x$ alloys. *Mater. Sci. Eng. A* **2010**, *527*, 6975–6979. [CrossRef]

17.　Miao, J.; Guo, T.; Ren, J.; Zhang, A.; Su, B.; Meng, J. Optimization of mechanical and tribological properties of FCC CrCoNi multi-principal element alloy with Mo addition. *Vacuum* **2018**, *149*, 324–330. [CrossRef]

18.   Nilsson, J.O.; Kangas, P.; Wilson, A.; Karlsson, T. Mechanical properties, microstructural stability and kinetics of σ-phase formation in 29Cr-6Ni-2Mo-0.38 N superduplex stainless steel. *Metall. Mater. Trans. A* **2000**, *31*, 35–45. [CrossRef]

19.   Lopez, N.; Cid, M.; Puiggali, M. Influence of o-phase on mechanical properties and corrosion resistance of duplex stainless steels. *Corros. Sci.* **1999**, *41*, 1615–1631. [CrossRef]

20.   Schwind, M.; Källqvist, J.; Nilsson, J.O.; Ågren, J.; Andrén, H.O. σ-phase precipitation in stabilized austenitic stainless steels. *Acta Mater.* **2000**, *48*, 2473–2481. [CrossRef]

21.   Tsau, C.H.; Tsai, M.C. The effects of Mo and Nb on the microstructures and properties of CrFeCoNi (Nb, Mo) alloys. *Entropy* **2018**, *20*, 648. [CrossRef]

22.   Chou, Y.; Yeh, J.; Shih, H. The effect of molybdenum on the corrosion behaviour of the high-entropy alloys $Co_{1.5}CrFeNi_{1.5}Ti_{0.5}Mo_x$ in aqueous environments. *Corros. Sci.* **2010**, *52*, 2571–2581. [CrossRef]

23.   Zhang, L.; Yu, P.; Zhang, M.; Liu, D.; Zhou, Z.; Ma, M.; Liaw, P.; Li, G.; Liu, R. Microstructure and mechanical behaviors of GdxCoCrCuFeNi high-entropy alloys. *Mater. Sci. Eng. A* **2017**, *707*, 708–716. [CrossRef]

24.   Li, T.; Liu, B.; Liu, Y.; Guo, W.; Fu, A.; Li, L.; Yan, N.; Fang, Q. Microstructure and mechanical properties of particulate reinforced NbMoCrTiAl High Entropy based composite. *Entropy* **2018**, *20*, 517. [CrossRef]

25.   Wu, C.; Zhang, S.; Zhang, C.; Zhang, H.; Dong, S. Phase evolution and cavitation erosion-corrosion behavior of $FeCoCrAlNiTi_x$ high entropy alloy coatings on 304 stainless steel by laser surface alloying. *J. Alloys Compd.* **2017**, *698*, 761–770. [CrossRef]

26.   Qiu, X.W.; Liu, C.G. Microstructure and properties of $Al_{2}CrFeCoCuTiNi_x$ high-entropy alloys prepared by laser cladding. *J. Alloys Compd.* **2013**, *553*, 216–220. [CrossRef]

27.   Lee, C.; Chang, C.; Chen, Y.; Yeh, J.; Shih, H. Effect of the aluminium content of $Al_xCrFe_{1.5}MnNi_{0.5}$ high-entropy alloys on the corrosion behaviour in aqueous environments. *Corros. Sci.* **2008**, *50*, 2053–2060. [CrossRef]

28.   Xiao, D.; Zhou, P.; Wu, W.; Diao, H.; Gao, M.; Song, M.; Liaw, P. Microstructure, mechanical and corrosion behaviors of AlCoCuFeNi-(Cr, Ti) high entropy alloys. *Mater. Des.* **2017**, *116*, 438–447. [CrossRef]